Stellar Occultations at UV Wavelengths by the SPICAM Instrument: Retrieval and Analysis of Martian Haze Profiles

Franck Montmessin, Eric Quémerais, Jean-Loup Bertaux, Oleg Korablev, Pascal Rannou, Sébastien Lebonnois

▶ **To cite this version:**

Franck Montmessin, Eric Quémerais, Jean-Loup Bertaux, Oleg Korablev, Pascal Rannou, et al.. Stellar Occultations at UV Wavelengths by the SPICAM Instrument: Retrieval and Analysis of Martian Haze Profiles. Journal of Geophysical Research. Planets, 2006, 111 (E9), pp.E09S09. 10.1029/2005JE002662 . hal-00112449

HAL Id: hal-00112449
https://hal.science/hal-00112449v1

Submitted on 20 Aug 2020

HAL is a multi-disciplinary open access archive for the deposit and dissemination of scientific research documents, whether they are published or not. The documents may come from teaching and research institutions in France or abroad, or from public or private research centers.

L'archive ouverte pluridisciplinaire **HAL**, est destinée au dépôt et à la diffusion de documents scientifiques de niveau recherche, publiés ou non, émanant des établissements d'enseignement et de recherche français ou étrangers, des laboratoires publics ou privés.

Stellar occultations at UV wavelengths by the SPICAM instrument: Retrieval and analysis of Martian haze profiles

F. Montmessin,[1] E. Quémerais,[1] J. L. Bertaux,[1] O. Korablev,[2] P. Rannou,[1] and S. Lebonnois[3]

Received 9 December 2005; revised 14 June 2006; accepted 27 June 2006; published 9 September 2006.

[1] Observations made by the SPICAM ultraviolet spectrometer on board the Mars Express orbiter are presented. We focus on several hundreds of atmospheric profiles which have been collected over 3/4 of a Martian year by making use of the stellar occultation technique. The typical structure of the Martian haze possesses at least one discrete layer (60% of all cases) standing over an extended portion wherein opacity continuously increases down to the surface. Differences of morphology are, however, noted between profiles observed near the equator and profiles collected elsewhere. The Martian haze exhibits a pronounced seasonal signal manifested by variations of the maximum elevation at which particles are observed. For reasons related to both convective activity and changes in the hygropause level, cold regions display a much lower hazetop than warm regions. Using UV spectrometry data, we put constraints on haze microphysical properties. Vertical variations of particle size are keyed to variations of opacity; e.g., an increase of particle size is systematically observed near extinction peaks. This is the likely consequence of cloud formation which results into a local increase of particle cross section. Despite marked differences of aerosol profiles between low and high latitudes, haze properties above 60 km remain invariant, possibly reflecting the long-term presence of a background submicronic particle population. Several profiles have been analyzed in more detail to extract properties of detached cloud layers lofted above 40 km. Their optical depth ranges between 0.01 and 0.1 in the visible. Estimation of cloud particle size is technically restricted because of SPICAM wavelength sampling, but it generally yields a minimum radius value of about 0.3 μm, while several estimates are consistent with a robust 0.1–0.2 μm. This crystal size, significantly smaller than the 1 to 4 μm associated with recently classified type I and II clouds, suggests that a different class of clouds, henceforth type III clouds, can be extracted from our data. Observations made in the southern winter polar night indicate a very distinct aerosol behavior where particles are less abundant ($\tau < 0.1$), confined to lower heights (vertical profile consistent with a Conrath parameter exceeding 0.04) and made of particles having a radius on the order of 0.1 μm. This shows that the Martian polar night is a region with a very clean atmosphere and with a distinct type of aerosols.

Citation: Montmessin, F., E. Quémerais, J. L. Bertaux, O. Korablev, P. Rannou, and S. Lebonnois (2006), Stellar occultations at UV wavelengths by the SPICAM instrument: Retrieval and analysis of Martian haze profiles, *J. Geophys. Res.*, *111*, E09S09, doi:10.1029/2005JE002662.

1. Introduction

[2] Martian aerosols have attracted the attention of scientists since their effect on climate has been recognized [*Hess*, 1973; *Pollack et al.*, 1979]. Dust in suspension is overall the largest and most permanent source of diabatic heating since it absorbs solar radiation at blue wavelength and heats the atmosphere. Airborne dust usually forms a thin, reddish veil covering the planet. During storms, dust can become so abundant that surface features are no longer distinguished. In addition to mineral dust, particles of condensate origin have been also reported. Two major examples are usually given in the literature: the equatorial cloud belt [*Clancy et al.*, 1996] and polar hoods. Both are triggered by seasonal processes and both result from the condensation of water vapor into ice. The equatorial cloud

[1] Service d'Aéronomie, CNRS/UVSQ/IPSL, Verrières-le-Buisson, France.
[2] Space Research Institute (IKI), Moscow, Russia.
[3] Laboratoire de Météorologie Dynamique, CNRS/UPMC/IPSL, Paris, France.

Copyright 2006 by the American Geophysical Union.
0148-0227/06/2005JE002662

belt appears around aphelion as a result of the adiabatic cooling of wet tropical air masses. Polar hoods are initiated by atmospheric radiative cooling in mid to high latitudes during fall and winter. CO_2 is also known to condense and to form clouds. However, CO_2 cloud observations are sparse since their occurrence is restricted to extremely cold regions, i.e., essentially the polar night.

[3] Global monitoring using nadir observations [*Smith*, 2004; *Tamppari et al.*, 2000] has given a good sense of how aerosol abundance varies with time and space in the Martian atmosphere (we refer as to ''aerosol'' any suspended particle of mineral or condensate origin). The vertical structure of aerosols is, however, poorly documented despite its importance for the haze characterization. Aerosol profiles indicate how haze is layered, how high suspended particles can penetrate and thus how various and strong vertically propagating motions can be. On Mars, documenting the haze structure is needed to help improving General Circulation Models (GCM). Vertical distribution of dust controls thermal structure and thus affects predictions. Hence the lack of aerosol profile observations adds uncertainty to model simulations, especially in the polar night where light and temperature conditions complicate retrievals.

[4] Information on the haze structure nonetheless exists. Profiles of light observed at the Martian limb have been collected during the Mariner 9 and the Viking missions [*Anderson and Leovy*, 1978; *Jaquin et al.*, 1986]. Light scattered by particles has been detected at altitudes greater than 60 km, mostly during southern spring and summer, the preferred seasons for dust storms. In addition, almost every profile analyzed by *Jaquin et al.* [1986] shows the presence of at least one spike of reflectivity presumably associated with cloud particles brighter than mineral dust.

[5] Some profiles were also obtained during PHOBOS mission using solar occultation. This technique of observation is based upon the measurement of extinction (absorption + scattering) of a light source by species, in general those contained in an atmosphere, that are present along the optical path. Compared to generic limb or nadir observations of reflected sunlight, occultations only depend on the ability of atmospheric species to scatter light in the forward direction. This is a significant advantage since the scattering phase function of an aerosol at mid to high angles is highly affected by its shape. *Pollack et al.* [1995], *Tomasko et al.* [1999], and also *Markiewicz et al.* [1999] had to use a semiempirical method [*Pollack and Cuzzi*, 1980] designed to account for particle nonsphericity in order to fit curves of light scattered by Martian dust at various phase angles. In contrast, occultation data retrievals can be performed with simple use of Mie theory to give consistent estimates of particle sizes since spectral variation of extinction cross section weakly depends on the shape of aerosols [*Korablev et al.*, 1993; *Wolff and Clancy*, 2003]. Occultation technique thus proves extremely powerful at deriving microphysical properties of planetary atmospheres.

[6] This work presents stellar occultation data obtained by the SPICAM instrument (Spectroscopy for the Investigation of the Characteristics of the Atmosphere of Mars) on board Mars Express spacecraft. They have been collected for a period covering three quarters of a Martian year and represent the largest data set published on the structure of the Martian haze to date. It consists of 612 occultation sequences which have successfully yielded 500 haze profiles at nearly all latitudes. Because the instrument is sensitive even to the faint light emitted by stars in the darkness, it has allowed us to probe the deep Martian polar night, a region where haze and atmosphere in general are poorly documented. The UV-wavelength range covered by SPICAM is large and the resolution high enough to obtain constraints on the aerosol spectral behavior. The first part of the manuscript is dedicated to a presentation of the instrument and to the method used for data retrieval. In the following part, haze vertical profiles inferred from our measurements are discussed. Despite the variety of cases, we have attempted to summarize the haze behavior in a compact presentation of data. Then, we specifically discuss aerosol profiles suspected to have a cloud feature and which have been analyzed to obtain quantitative estimates of cloud properties. Finally, we focus on some profiles of the polar night that have been inverted to characterize haze opacity and structure in that particular region of Mars.

2. SPICAM Instrument

2.1. Overview

[7] SPICAM is a small ultraviolet-near infrared instrument which is part of the Mars Express mission payload. SPICAM includes two optical sensors and an electronic block. The UV imaging spectrometer covers the 118–320 nm wavelength range with a resolution of about 0.5 nm. It is dedicated to nadir and limb viewings, but can also perform occultations in a solar or in a stellar mode. The IR spectrometer covers the 1.0–1.7 μm range and is mostly dedicated to the characterization of the Martian surface properties and of specific atmospheric components (H_2O, O_2). Further details on the instrument are given by *Bertaux et al.* [2000, 2006].

[8] The UV channel of SPICAM is a full UV imaging spectrometer which spatially resolves 288 spectra along its slit. The light flux is collected by an off-axis parabolic mirror which reflects light toward the spectrometer entrance. At the focal plane, a mechanical slit system provides two configurations: without the slit for stellar occultations, and with a slit for extended source observation (such as the surface or the sun). When the slit is removed during a stellar occultation sequence, it creates a hole corresponding to the total useful field of view of $2 \times 3.16°$. Due to telemetry constraints, only 5 spectra can be transmitted per second of measurement. For this reason, spectra are first summed over n pixel lines (n = 16 in an occultation) before their transmission to Earth.

2.2. Data Inversion Technique

[9] The occultation technique relies on the determination of atmospheric transmission at various altitudes above the surface. Only relative measurements are needed to infer species abundances, and thus the method is self-calibrated. Since SPICAM is not equipped with a pointing system, an occultation sequence requires a change of spacecraft attitude to allow the instrument target a specific star and place it at the center of the CCD. Along the orbital trajectory of Mars Express, the spacecraft maintains this attitude long enough to let a spectrum be acquired both from outside and through the atmosphere. We consider the slant path to be outside the

atmosphere when the tangential altitude is sufficiently high (usually several hundreds of km) so that absorbing species are so scarce they do not affect the appearance of the light source. This is the altitude range at which a reference spectrum of the star is obtained. The ratio of spectra taken through and outside the atmosphere gives an atmospheric transmission at each altitude above the point on the surface that is closest to line of sight. This point drifts slowly enough during the sequence so as to be assumed fixed to first order. If any absorbing or/and scattering species are present along the optical path between the star and the spacecraft, photons are lost and resulting transmissions are lower than 1.

[10] The sampling frequency (1 Hz) yields a vertical resolution of 1 to 3 km. The sounded region inside which a quantity of atmospheric constituents can be derived lies generally between 20 and 140 km. Above 140 km, the signature of species is too weak and cannot be separated from instrumental noise. Below 20 km, the tangential opacity of the planetary haze is so large that SPICAM cannot collect any photon at any wavelength. SPICAM performances in this specific configuration depend on the quantity of photons emitted by the star. Signal to Noise Ratio (SNR) is respectively greater than 91 and than 29 per pixel for two levels of star emission (respectively 10^4 and between 10^3 and 10^4 phot.s^{-1}.cm^{-2}, as derived from Henry formulas). CO_2, O_3 and aerosol spectral signatures cover a spectral range corresponding to more than 100 pixels.

[11] A posttreatment is performed on spectra to subtract dark current and the systematic offset added to CCD output to avoid negative voltages at the entrance of the A/D converter. This procedure along with the data inversion method are described in greater detail in a companion paper [*Quémerais et al.*, 2006]. An example of raw data is displayed in Figure 1a. It is representative of the usual "tempo-spectrum" (named after the (λ, t) coordinate system into which data are projected) obtained by SPICAM during a stellar occultation sequence. Spectral signatures of ozone and carbon dioxide are readily apparent. At each altitude, a transmission spectrum is fitted using the following function:

$$T_{fit}(\lambda) = \exp\left(-Q^{co2}\sigma_{co2}(\lambda) - Q^{o3}\sigma_{o3}(\lambda) - \tau_{aer}(\lambda)\right) \quad (1)$$

where Q^{co2}, Q^{o3} are the number of CO_2 and O_3 molecules along the line of sight per unit surface, and τ_{aer} is the slant opacity of aerosols. σ_{co2}, σ_{o3} are the wavelength-dependent extinction coefficients for carbon dioxide, ozone. CO_2 and O_3 have each a distinct absorption feature respectively shortward of 200 nm and around 250 nm. Absorption coefficients for gases come from a compilation of laboratory data [*Yoshino et al.*, 1996; *Parkinson et al.*, 2003]. CO_2 absorption has only been measured at 195 K and 295 K, and thus does not cover the potential range of thermal conditions of the upper atmosphere. However, it only mildly affects the shape of the CO_2 absorption feature and thus is of no consequence for aerosol abundance retrieval.

[12] Whereas spectral behaviors of CO_2 and water ice crystals can be computed using laboratory data [*Warren*, 1984, 1986], Martian dust properties are not well constrained in UV. *Ockert-Bell et al.* [1997] derived refractive indices from ultraviolet to near-infrared but indicate that their values differ significantly from a previous work [*Pang and Ajello*, 1977] and admit that "ultraviolet interaction with the dust is problematic." With all the data collected by SPICAM, it should be possible to help work out this discrepancy in a near future. To fit the continuum optical depth, we use an approximation employed on Earth to represent the spectral behavior of aerosols in an absorptive regime [*O'Neill and Royer*, 1993; *Dubovik et al.*, 2000]:

$$\tau_{aer}(\lambda) = \tau_{\lambda o}(\lambda_o/\lambda)^{\alpha} \quad (2)$$

where λ_o is a reference wavelength and where α is known as the Angström coefficient. We will refer this approximation as to the α-model (note that in the companion paper of *Rannou et al.* [2006] the α-model is also employed in the retrieval of SPICAM limb observations, but the convention for the sign of α is opposite to ours). This approximation is particularly convenient as only one parameter, α, is needed to describe the wavelength dependence of aerosol extinction. Yet, it proves highly consistent (see Figure 2 for a demonstration). As shown by Figure 2d, α is larger when particles are smaller, a statement only verified for those particles whose sizes are comprised between 30 and 300 nm. Below 30 nm and in case of dust, the α-model significantly deviates from a spectral behavior predicted by Mie theory used here as a reference. Angström values derived in this size range are unlikely to be valid for dust particles. Around 200–300 nm, the α-model is again too simplistic to reproduce Mie theory, but the approximation can still be considered reasonable (see the comparison between our model and Mie theory displayed in Figures 2a, 2b, and 2c). Above 300 nm, particle size cannot be discriminated as it enters a regime dominated by constructive and destructive interferences resulting in the well-known Mie oscillations. At larger sizes, the spectral dependence becomes neutral since extinction efficiency asymptotes around 2, the value predicted by geometrical optics. This explains why the corresponding α values fluctuate around zero above 300 nm.

[13] Most studies agree on a Martian dust particle size distribution exhibiting an effective radius (cross-section weighted mean radius of the particle population) between 1 and 2 μm [*Pollack et al.*, 1995; *Tomasko et al.*, 1999; *Clancy et al.*, 2003; *Korablev et al.*, 2005]. SPICAM UV cannot discriminate micron-sized particles since they have no spectral slope in UV (α = 0). However, at the altitudes probed by the instrument, sedimentation is effective at sorting out larger particles, leaving only smaller ones. Even if SPICAM stellar occultations are not well designed to characterize the bulk of Martian dust which lies in the lowest layers of the atmosphere, it is well suited to detect and discriminate submicron particles which may be more frequent at higher altitude. Because of its sensitivity to ultraviolet, SPICAM nicely complements Martian aerosol observations made by previous instruments at longer wavelengths.

[14] The fitting procedure is based on a Levenberg-Marquardt algorithm (IDL-based MPFIT routines created by C. Markwardt: http://cow.physics.wisc.edu/~craigm/idl/idl.html) which simultaneously adjusts the following four parameters: Q^{co2}, Q^{o3}, $\tau_{\lambda o}$ and α. Values returned at every altitude are compiled to determine the resulting vertical

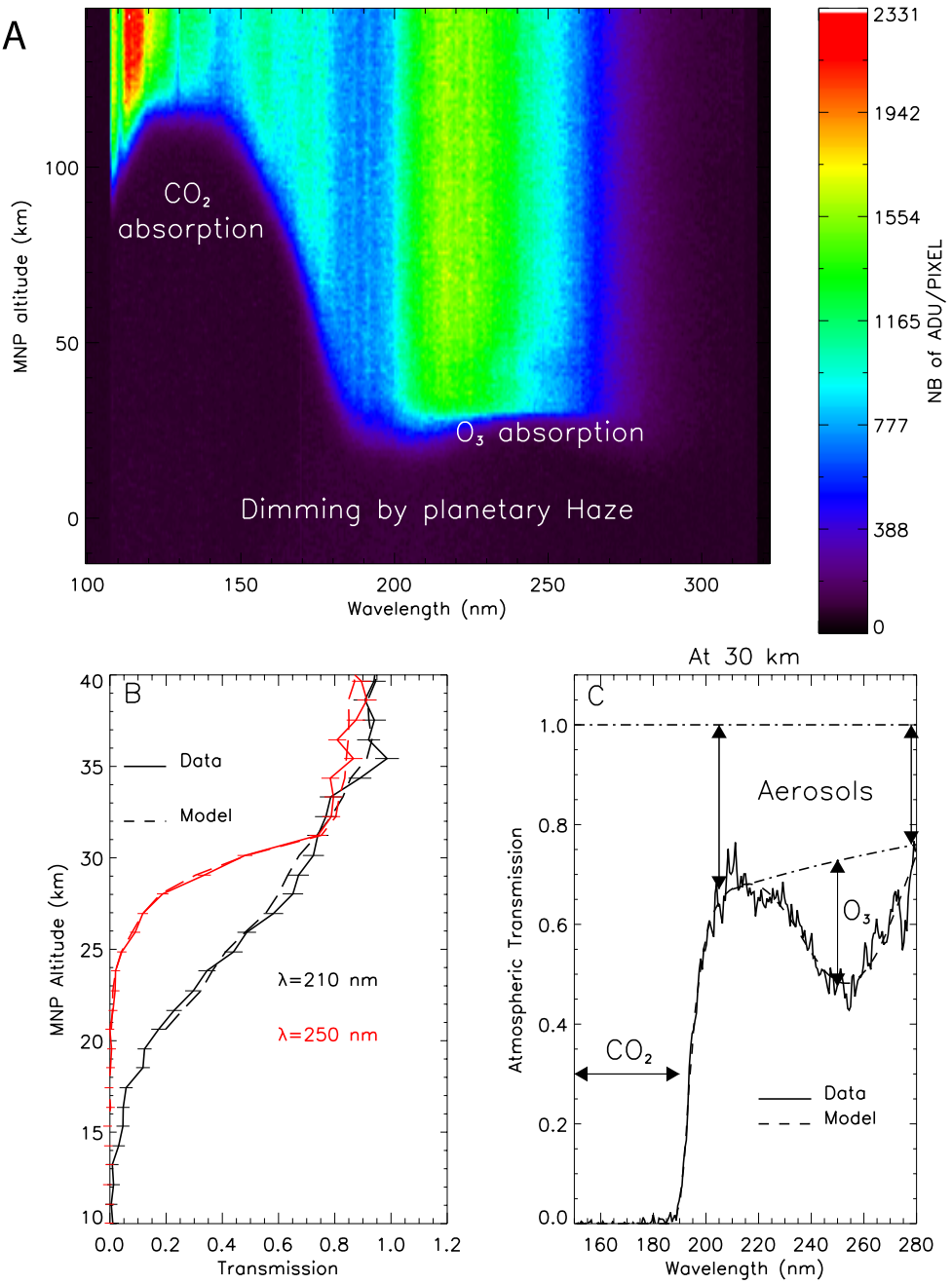

Figure 1. (a) Tempo-image derived from orbit 947. Photon counts (shown here as Analog to Digital Units (ADU)) are plotted as a function of wavelength and of the Mars Nearest Point (MNP) altitude. MNP altitude is defined above a reference Martian geoid and is equal to the altitude of the point at which the SPICAM line of sight is tangential to the atmospheric shell. Lyman-α emission by H atoms are detected around 120 nm and above 120 km. Below this altitude, EUV absorption by CO_2 molecules dominates the signal shortward of 180 nm. O_3 can also be distinguished as it attenuates photon counts shortward of 250 nm between 30 and 60 km. Atmospheric species can be derived down to 30 km. From the ground up to this height, aerosols are too abundant to let the star be sighted. (b) For the same orbit, a comparison of transmission profiles at two UV wavelengths. Modeled transmissions are plotted against data values with their corresponding error bars. (c) An example of transmission spectrum and its corresponding fit. The spectrum was collected at an altitude of 30 km, where the signatures of the three species of interest can be easily identified: (1) CO_2, (2) O_3, whose absorption creates a trough of transmission between 200 and 280 nm, and (3) aerosols, which interfere at all wavelengths. As indicated by the dashed line, aerosol opacity decreases rapidly with increasing wavelength, reflecting a α value greater than 2.

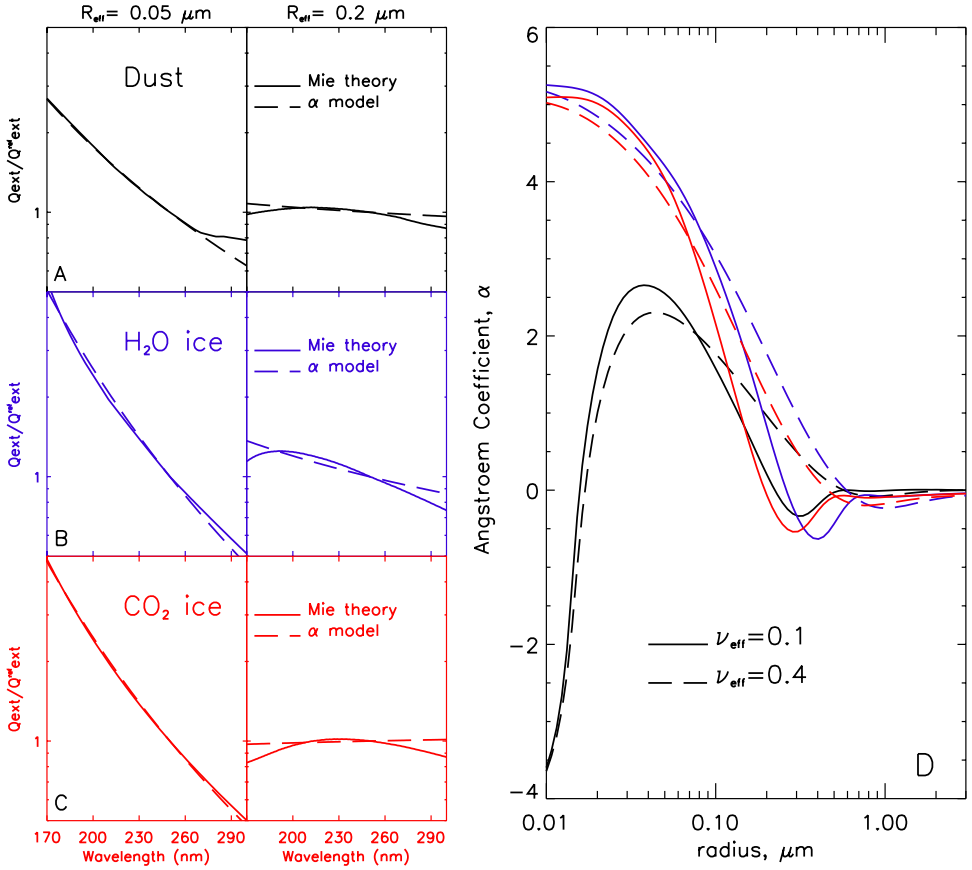

Figure 2. Spectral behavior of (a) dust, (b) H_2O, and (c) CO_2 ice particles in the UV wavelength region sounded by SPICAM. The quantity displayed is the extinction efficiency scaled by its value at a reference wavelength of 250 nm. Two cases are plotted: one is computed using Mie theory; the other is given by fitting the previous with the α-model (see text for details). For an effective radius of 50 nm, the fit is good whatever the composition. The quality is reduced at larger sizes, here for a radius value of 200 nm (right-column plots). When particle size is comparable to wavelength, constructive and destructive interferences give rise to the so-called Mie oscillations. Such spectral behavior cannot be reproduced by the simplistic α-model. (d) Angström coefficients (α) plotted as a function of the cross-section weighted average radius of a log-normal population of dust particles. Values are derived by fitting the extinction efficiency predicted by the Mie theory in the SPICAM ultraviolet range. Two types of curves (dashed and solid) are plotted as two different effective variances ν_{eff} were assumed (0.1 and 0.4). However, it is evident that the influence of ν_{eff} on α is secondary compared to the dominant effect of changing radius. Color coding is the same as in left plots.

profile of each species (see *Lebonnois et al.* [2006] for a discussion on ozone data retrieval). The absolute accuracy of the retrieved species abundances generally ranges around 5%. It is difficult to evaluate the error induced by approximating the contribution of aerosols to signal. The α-model has nonetheless proven reliable for many terrestrial studies and generally offers a good estimation of aerosol behavior. Modeled spectra have been carefully compared to original data. In most cases, the fit quality is very high, but some anomalous behaviors have been identified, in which cases the fitting attempt was abandoned and no species abundance was retrieved. Figure 1c shows a comparison between a fitted transmission spectrum and a transmission derived from actual data. It has been chosen to illustrate the prominent signatures of CO_2 and O_3 and to show the transmission reduction due to aerosols over the whole spectral range. A comparison between modeled and observed transmission vertical profiles at specific wavelengths is given in Figure 1b to illustrate the consistency of the fitting procedure.

3. Results

[15] Since the very first occultation sequence made on the 01/13/2004, more than 600 profiles have been collected by SPICAM. A number of sequences has been lost due to, e.g., pixel saturation, spacecraft mispointing, contamination by stray light. Some sequences were also rejected because of an anomalous spectrum behavior generally caused by spurious spacecraft oscillations. Nearly five hundred sequences have been consistently treated and have yielded vertical profiles of atmospheric species. The data set spans a period starting at the end of northern winter (at L_s = 330°, which corresponds to the arrival of Mars Express at Mars) and finishing near northern winter solstice (Ls = 270°). As shown by Figure 3, most observations have been performed in the

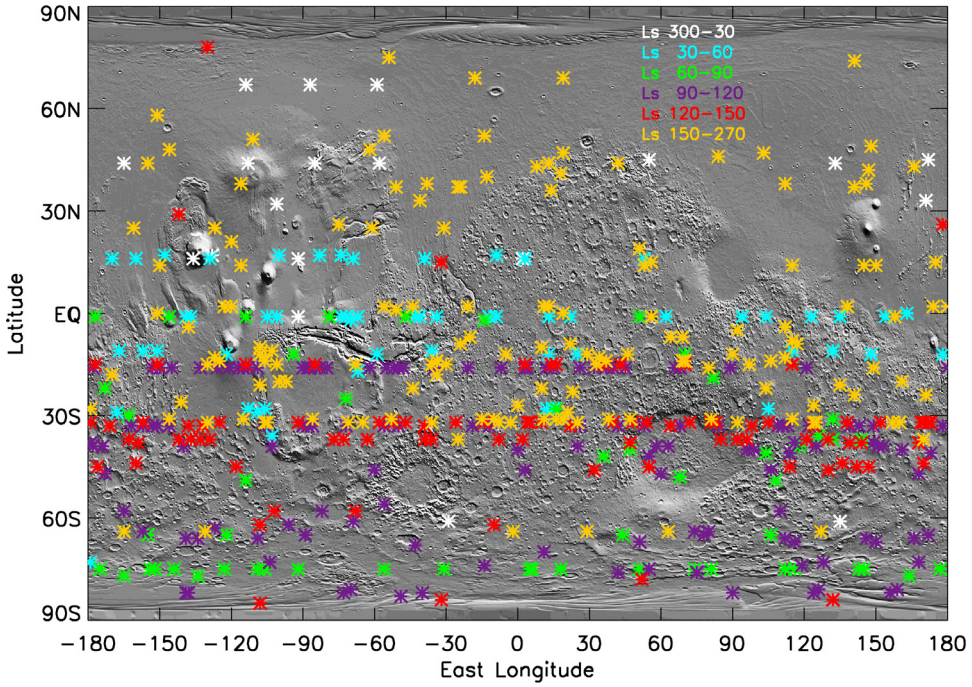

Figure 3. A MOLA map of the Martian surface showing the locations of the Mars nearest point along the line of sight for all processed occultations. Color coding refers to the season of observation as indicated in the figure.

southern hemisphere, and especially within three latitudinal annuli: 15°S, 30°S and 75°S.

3.1. Detection of a Seasonal Signal

[16] Using limb profiles in the visible, *Jaquin et al.* [1986] showed that the hazetop (the maximum elevation at which aerosols are detected) at low latitudes gradually increases from aphelion ($L_s = 70°$) to perihelion ($L_s = 250°$). The same analysis has been conducted with our data set, using a threshold value of 0.1 as the minimum aerosol slant opacity (at λ = 250 nm) above which particles are considered present along the line of sight. Resulting seasonal variations of hazetop as monitored by SPICAM are plotted in Figure 4 and in Figure 5 (in the latter, hazetop is displayed as a function of both season and latitude). Our results corroborate previous Viking observations and show again strong variations of the Martian haze associated with seasons. At first glance, variations seem related to the influence of the eccentric Martian orbit. Data can indeed be fitted by a cosine function, whose expression is displayed in Figure 4, and which have a periodicity of about one Martian year, with the hazetop minimum occurring near aphelion. In reality, data variations are also caused by spacecraft periapsis drifting latitudinally during the mission. Since the latter has consequences for spatial sampling, the decrease of hazetop around aphelion is also the result of the spacecraft periapsis progressively moving to the colder high latitudes of the southern fall hemisphere. The following increase corresponds to a return to warmer equatorward latitudes. In any case, differences of hazetop altitude look correlated to thermal contrasts, be it seasonal or geographic.

[17] This relation between haze and temperature can be explained by two separate yet combined effects:

[18] 1. First, with reduced insolation comes weaker convective activity and thus less capacity for the atmosphere to maintain particles higher up. Warmer regions are therefore more prone to exhibit elevated hazetops.

[19] 2. The second effect is the result of changes in water condensation level. Since cloud particles likely form onto mineral dust aerosols, their subsequent fall scavenges dust to lower heights. Cloud levels therefore set an upper limit above which dust hardly propagates. Temperature changes modulate the saturation level and thus the altitude of cloud formation, which in turn controls the maximum elevation of the dusty haze layer.

3.2. Typical Haze Morphology and Microphysical Properties

3.2.1. Correlations Between Size and Opacity

[20] Every fitted spectrum yields a value for the Angström coefficient, and thus an information on particle size. However, size estimation is linked to our assumption of spherical particles (Mie theory). Real dust or icy grains are probably far from perfect spheres, but this aspect should mildly affect our conclusions. The demonstration is made by *Wolff and Clancy* [2003] that differences of extinction cross section, which is an intrinsic forward scattering quantity and which is the only quantity measured by SPICAM during an occultation, between spheres and spheroids are almost negligible, regardless of the size parameter ($2\pi r/\lambda$). This is due to the fact that particle shape essentially affects aerosol phase functions at scattering angles $\geq 40°$ [*Dubovik et al.*, 2000; *Wolff and Clancy*, 2003], but has limited impact on the forward scattering lobe.

[21] As shown by Figure 6, we have been able to determine that a relation exists between a haze opacity profile and its corresponding profile of particle size (using

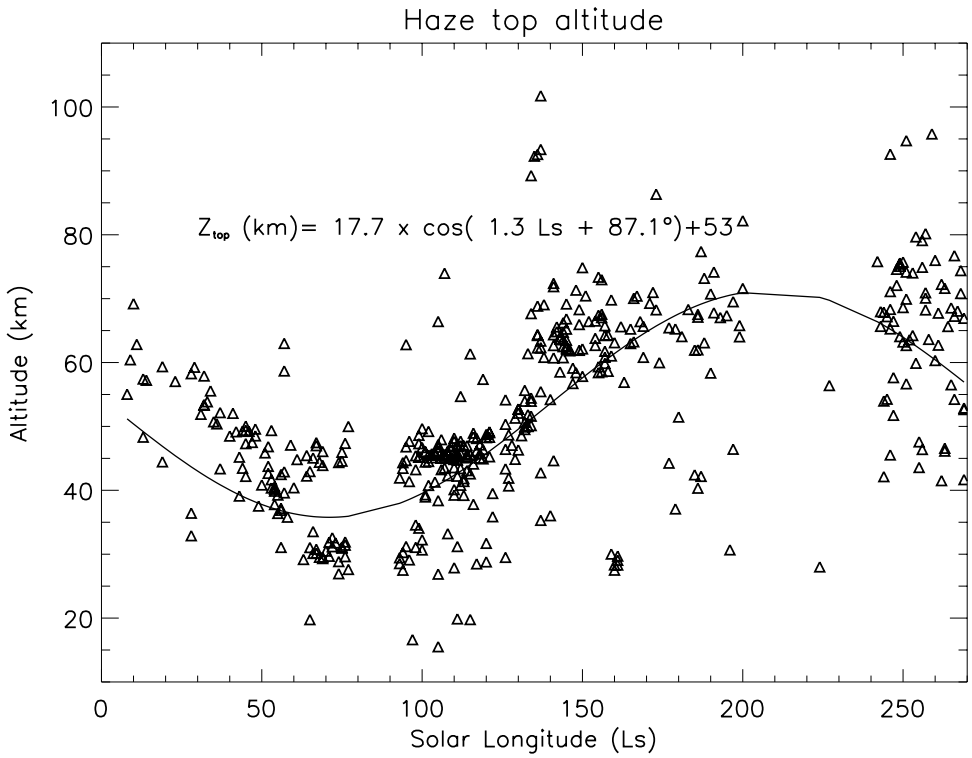

Figure 4. Seasonal variations of the hazetop as derived from SPICAM aerosol profiles. Data have been fitted by a cosine function whose expression is given in the figure. The periodic signal is phased essentially with the seasonal sampling imposed by the latitudinal drift of the spacecraft periapsis.

α values as a proxy). Two pieces of information can be drawn from this figure:

[22] 1. A vertical decrease of opacity with increasing altitude corresponds to a reduction of particle size. Figure 6 indicates that in case of negative variations of opacity ($d\tau/dz < 0$), plots concentrate in the positive part of α variations ($d\alpha/dz > 0$).

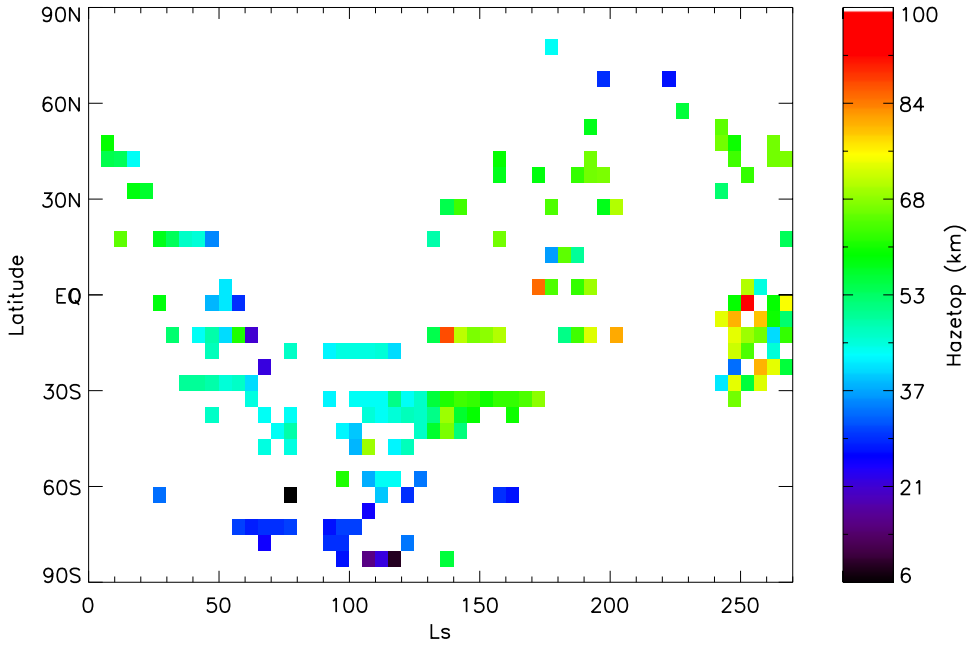

Figure 5. Seasonal variations of the hazetop as a function of latitude. Values have been averaged in boxes of 5° in L_s and 5° of latitude. Despite the uneven spatial coverage, it is perceptible that low-latitude to midlatitude regions experience a significant hazetop increase from aphelion to perihelion seasons. This trend is likely the result of a climatic asymmetry generated by the eccentric orbit of Mars.

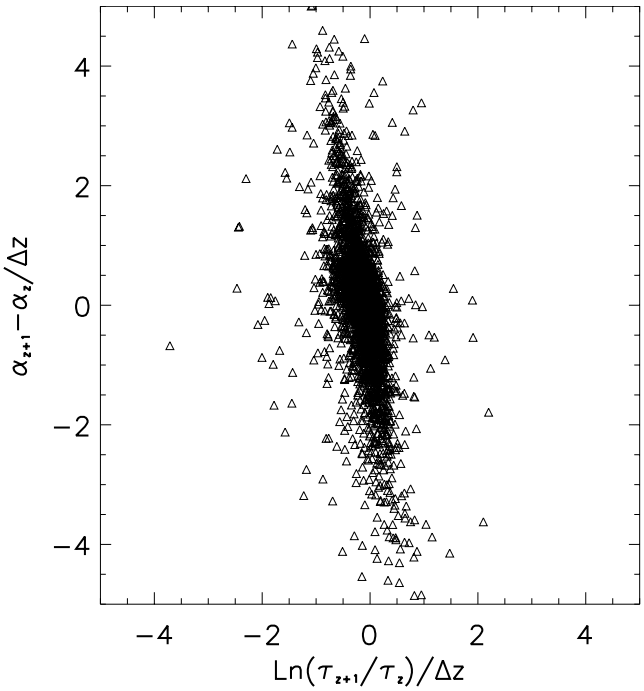

Figure 6. Vertical variations of particle size plotted against the vertical variations of aerosol slant opacity. Variations were computed between two adjacent atmospheric levels throughout all the profiles collected by SPICAM. For opacity, we use $\ln(\tau_{z+1}/\tau_z)/\Delta z$, where Δz is the altitude difference between two atmospheric levels, τ_{z+1} is the aerosol slant opacity at a level $z + 1$, and τ_z is that at level z. Particle size vertical variation is expressed by $(\alpha_{z+1} - \alpha_z)/(\Delta z)$, where α_{z+1} is the value of the Angström coefficient derived at a level $z + 1$ and α_z is that derived at z. The elongated shape of the cloud of points confirms that the two quantities are correlated. We could have used quantities obtained after vertical inversion in order to access local variations, but this procedure adds numerical noise and only amplifies structures that are already present in slant opacity profiles.

[23] 2. When opacity increases with height, so does particle size.

[24] These statements are only meaningful in a statistical sense, and are not verified systematically at the scale of isolated points. Item 1 is the expected consequence of sedimentation. Settling velocity increases with particle size and with increasing height (rarefied air offers less resistance to particle motions). Sedimentation subsequently forces both aerosol mass and size to decrease with increasing height. Item 2 is related to cloud occurrences. Because of condensation, crystals become much larger than their initial dust nuclei. A local increase of both opacity and particle size is thus expected where a cloud forms. This is well illustrated by profiles 956, 1073 and 1079 displayed in Figure 8.

3.2.2. Properties of the Average Martian Haze Profile

[25] Data have been averaged to yield representative haze profiles (displayed in Figure 7) for two latitudinal sectors chosen for their distinct regimes: (1) between 15°S and 15°N and (2) poleward of 15°. Around the equator, haze appears confined to lower heights and exhibits greater opacity. The gradual increase of opacity from bottom to top suggests a dominant affect of sedimentation and mixing on the overall structure. The average Angström coefficient profile is roughly constant up to 55 km and then increases up to 80 km. Poleward of 15°, the haze is less confined and displays a prominent spike around 55 km, the likely result of recurrent cloud layers. Differences between the two latitudinal sectors are also noted for the Angström coefficients which are slightly shifted to higher values in the >15° latitude profile, suggesting the presence of substantially smaller particles.

[26] We have estimated the size of particles using the equivalence between radius and Angström coefficient displayed in Figure 2. As indicated in Figure 7, the atmospheric region above 60 km is populated by submicron particles ($r_{eff} < 0.1$ μm) at all latitudes. We interpret this feature as the presence of a background population of very fine aerosols, probably dust, that are long-term stable at high altitude where micron-sized grains cannot remain aloft. Below 50 km near the equator, particle size can no longer be discriminated as sizes are larger than 0.3 μm in radius ($\alpha \sim 0$). This is consistent with previous observations where a particle radius of 0.8 μm was inferred at 25 km in the equatorial region [*Korablev et al.*, 1993].

3.3. Properties of the Detached Layers

[27] Statistics based on a visual inspection of profiles morphology reveal that more than 60% of occultation sequences exhibit at least one discrete layer probably of condensate origin, although a dust plume cannot be excluded. Detached layers were also a common feature in Viking limb images [*Jaquin et al.*, 1986].

[28] We have selected several sequences where detached layers possess a well-defined structure and have used them for further analysis (these occultation profiles are presented in Figure 8). Opacity profiles have been first processed through vertical inversion to obtain subsequent extinction profiles (Figure 9). Then, extinction has been integrated over the vertical extent of the detached layer to estimate the total cloud optical depth. For the sake of comparison with previous observations, extinction coefficients have been spectrally extrapolated using corresponding Angström values and equation (2) to get cloud opacity at visible wavelength. All cloud characteristics are summarized in Table 1. Because SPICAM is blind below 20–30 km, our observations mostly sample clouds forming above 40 km. On average, cloud opacity ranges from 0.01 to 0.1 in UV and should lie near the same value in the visible since layers have a neutral spectral behavior. Cloud vertical extent usually exceeds 10 km, reaching 30 km in some cases. Although differences in cloud vertical extent should give good indications on convective strength variations, no clear pattern could be drawn from our data set. Corresponding Angström coefficients generally lie in a range where our retrievals lose sensitivity to particle size, which suggests ice crystal radii greater than 0.3 μm. We also distinguish several cases with a pronounced spectral behavior that can be robustly associated with a radius value of 0.1–0.2 μm.

3.4. Multilayer Profiles

[29] Some profiles exhibit multiple discrete layers (see Figure 10). These occurrences are restricted to mid southern latitudes and are not connected to any particular topographic feature. Similar structures have been reported during Pho-

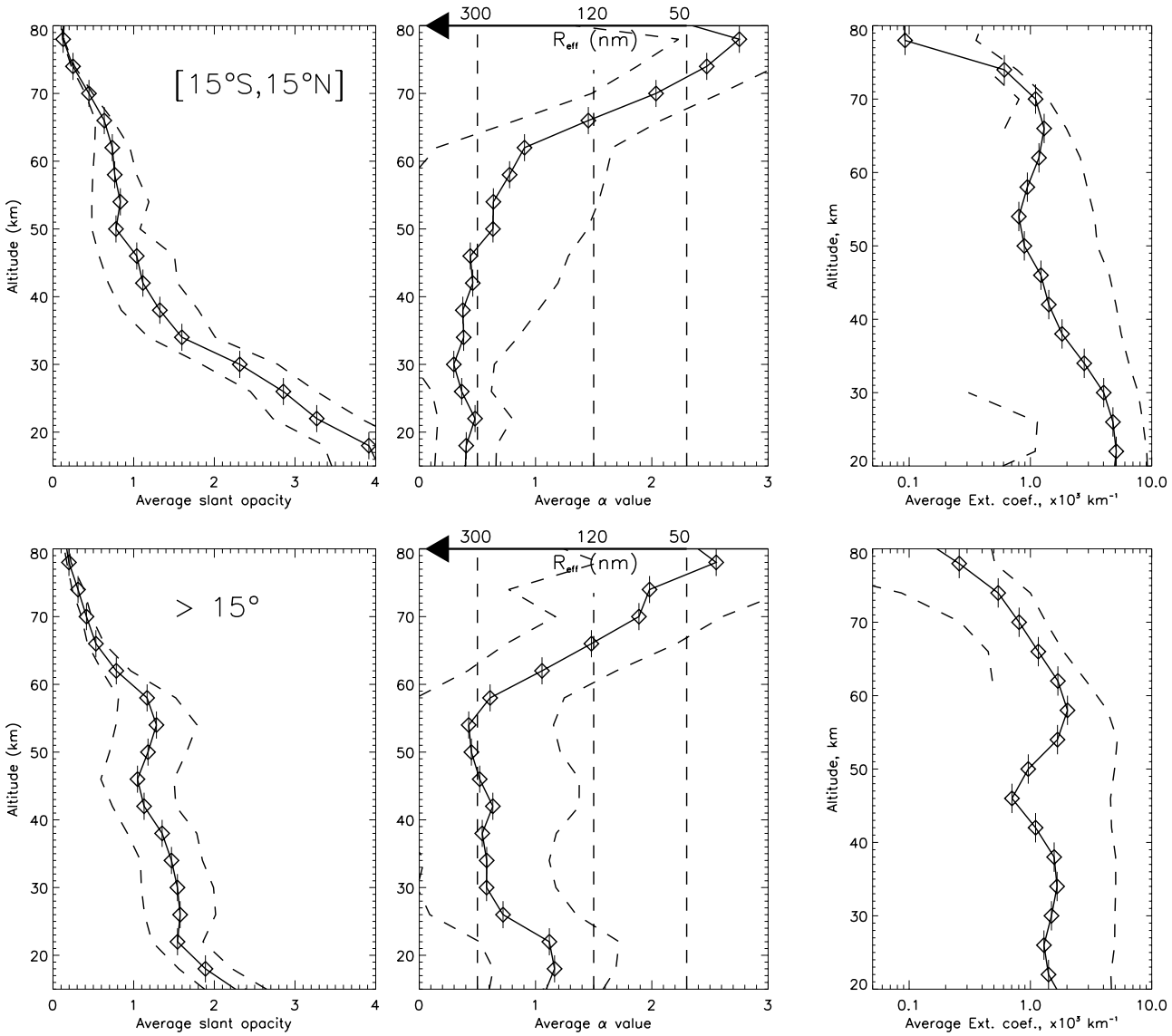

Figure 7. Top plots: Aerosol slant opacity at (left) 250 nm, (middle) Angström coefficient, and (right) extinction coefficient profiles obtained after averaging all occultation data inside 4 km atmospheric slices (shown by the small vertical bars assigned to each point). Extinction profiles are computed with a vertical inversion of the average slant opacity values. Profiles are representative of the near-equator region extending between 15°N and 15°S. Dashed curves indicate the range of standard deviation of data from their average and thus show data natural variability. The top axis of the right-hand profile indicates the range of particle radius equivalent to that of the Angström coefficient on the bottom axis. Bottom plots: Same as above except for the regions poleward of 15° in both hemispheres.

bos mission and have been interpreted as cloud layers stacked one above the other [*Chassefiere and Blamont*, 1992]. Such a vertical structure can be produced by a strong updraft added to a thermal inversion layer located between the two cloud levels [*Chassefiere and Blamont*, 1992]. In such case, water ice crystals carried upward from the lowest cloud sublimate and release water vapor while traveling through the thermal inversion layer. Released water vapor is then available to be supplied to the highest cloud.

[30] Another explanation is provided by mesoscale modeling which shows that volcano-induced thermal circulation is capable of injecting huge amounts of dust that can create plume layers above 30 km [*Rafkin et al.*, 2002]. It is thus possible that multilayer profiles observed by SPICAM are a consequence of local intense updrafts located near volcanoes.

3.5. Profiles Collected in the Polar Night

[31] Stellar occultation technique allows to survey dark regions. On Mars, this is of particular interest since a crucial part of climate is played in the polar night regions where surface temperature falls below CO_2 condensation point during fall and winter. CO_2 condenses out on the ground and releases latent heat so as to balance cooling due to surface emission to space. This is one of the most salient phenomena of the Martian climate which is known to induce significant seasonal variations of global pressure.

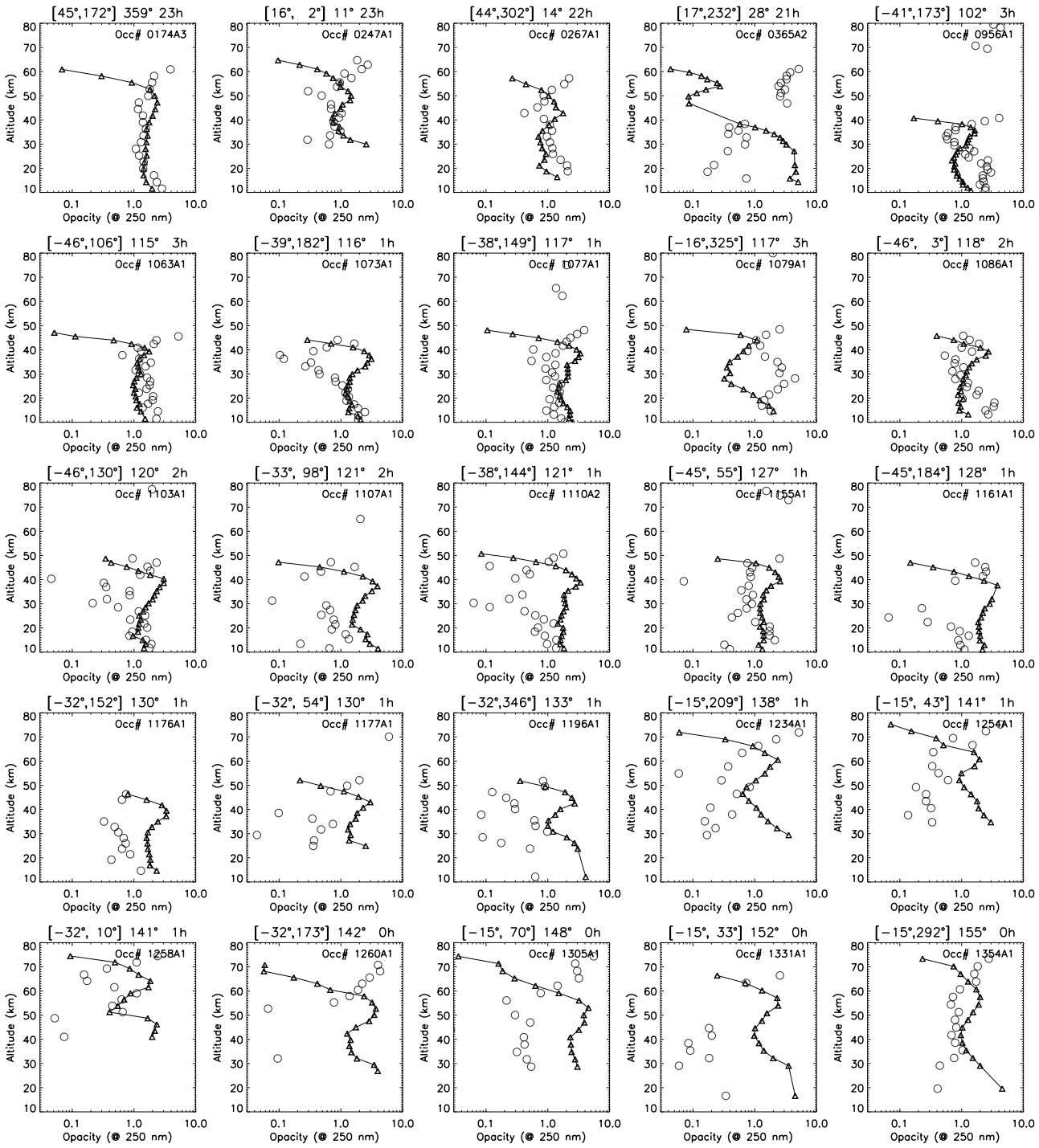

Figure 8. A selection of haze vertical profiles observed by SPICAM which show a prominent detached layer structure in their upper portion. Solid curves give the slant opacity of aerosols at a wavelength of 250 nm. Circles indicate the corresponding values of Angström coefficients and are plotted over the same scale. Above each graph, latitude and longitude are given in that order between brackets. The following numbers indicate the solar longitude and the local time of observation at the tangential point.

Unfortunately, this aspect of Mars climate is incompletely documented. While atmospheric temperatures have been retrieved from IR measurements [*Smith et al.*, 2001] and radio occultations [*Hinson et al.*, 2003], almost no information refers to aerosols, except for one profile collected by TES near 80°N and discussed by *Pearl et al.* [2001]. Polar night haze has strong implications for climate since aerosols can change IR emission to space and can therefore alter the amount of CO_2 condensing in the atmosphere. Aerosol IR emission should also perturb latitudinal temperature gradients between mid and high latitudes and this may have consequences for the intensity of planetary-scale waves

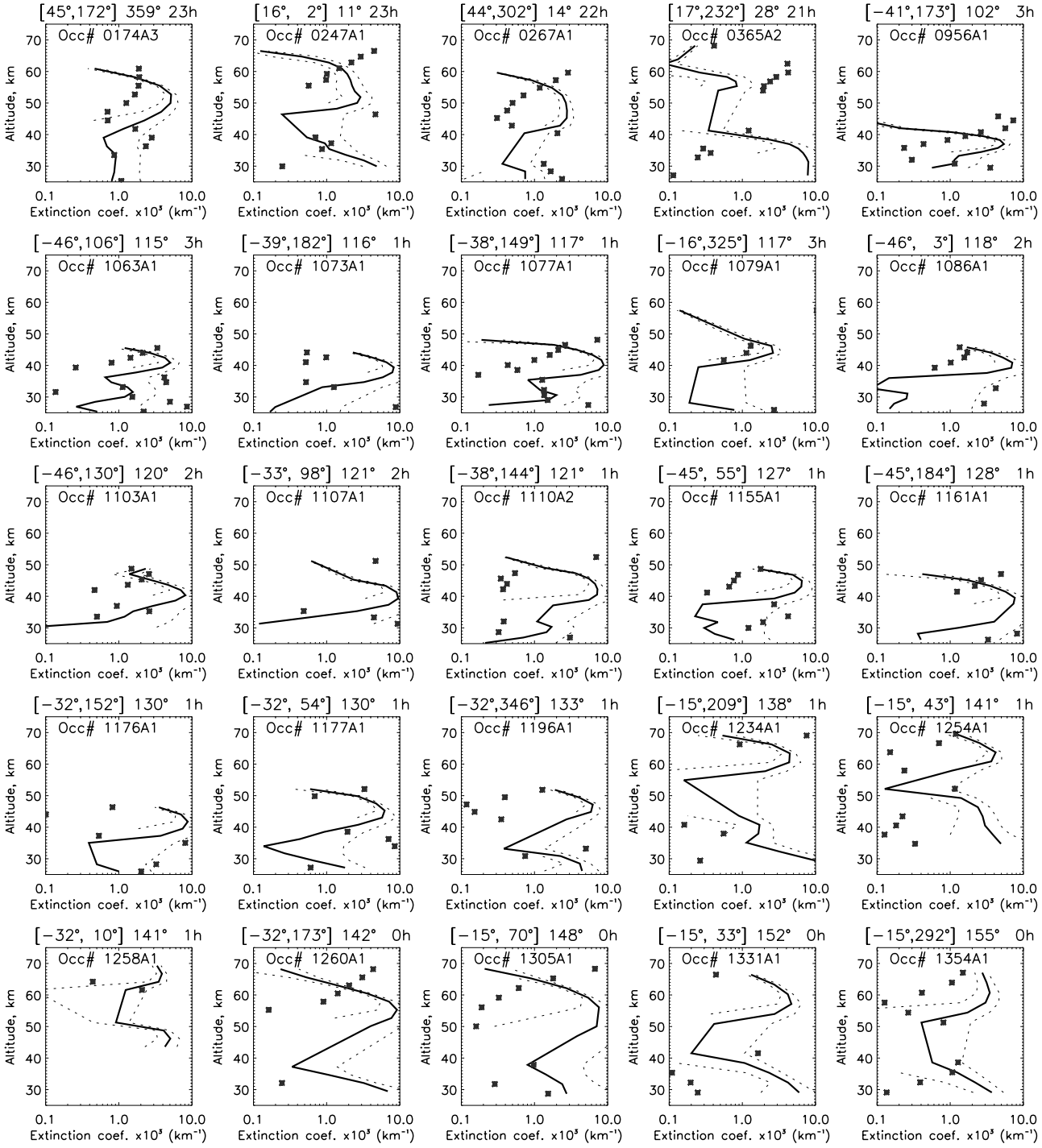

Figure 9. Extinction profiles (bold lines) obtained from the vertical inversion of the opacity profiles that are displayed in Figure 8. An envelop of 1σ-uncertainty is represented by dotted curves. Symbols give the Angström coefficient values (same scale as opacity).

(J. Hollingsworth, personal communication, 2005). In addition, studies conducted in a theoretical framework have concluded on the possibility of CO_2 convective clouds associated with the rapid release of latent heat during atmospheric condensation episodes [*Colaprete et al.*, 2003].

[32] Occultations performed so far restrict our study to the south polar night with related profiles displayed in Figure 11. A subset of occultations has been further inverted to yield the vertical distribution of aerosol extinction (Figure 12). These measurements exhibit a remarkably recurrent structure which differs significantly from that of profiles collected at other places on the planet. Polar nights are where SPICAM could access the lowest tangential altitudes (10 km and even below), implying that aerosols are strongly confined and/or in low quantity. Most profiles exhibit a low hazetop (located around 30 km) and a monotonous morphology wherein discrete layers are almost absent. Vigorous convective motions associated with CO_2 cloud formation are not neces-

Table 1. Summary of Cloud Layer Properties Derived From Figure 9

Orbit	Lat	Lon	Ls	Local Time	z_{max}[a] km	σ_{max},[a,b] $\times 10^3$/km	α[a]	R_{eff},[a] μm	Δz,[c] km	τ_{250}/τ_{500}[d] ($\times 100$)
0174A3	45	172	359	23^h	53	5.2	1.6	0.15	21	6.5/2.6
0247A1	16	2	11	23^h	52	2.9	−0.3	>0.3	20	3.5/2.7
0267A1	44	−58	41	22^h	48	2.8	0.4	0.3	20	4.4/2.6
0365A2	17	−128	28	21^h	55	0.8	2	0.12	10	0.8/0.2
0956A1	−41	173	102	03^h	37	5.4	0.4	0.3	10	3.1/2.1
1063A1	−46	106	115	03^h	41	5	0.8	0.2	10	3/1.6
1073A1	−39	−178	116	01^h	39	8.3	0.04	>0.3	10	6.3/5.2
1077A1	−38	149	117	01^h	40	8.8	0.4	0.3	15	6.7/3.6
1079A1	−16	−35	117	03^h	44	2.7	1.1	0.18	15	2.4/1.5
1086A1	−46	3	118	02^h	41	7	1	0.18	10	4.5/2.5
1103A1	−46	130	120	02^h	40	8.1	−0.3	>0.3	15	6.4/4.7
1107A1	−33	98	121	02^h	39	9.5	−0.8	>0.3	25	8.3/10.8
1110A2	−38	144	121	01^h	42	7.3	0.3	>0.3	20	7.5/8.6
1155A1	−45	55	127	01^h	45	6.5	0.8	0.2	15	5.3/3.4
1161A1	−45	−176	128	01^h	40	7.6	0	>0.3	20	8.2/13.2
1176A1	−32	152	130	01^h	41	8.8	−0.3	>0.3	10	7.0/6.8
1177A1	−32	54	130	01^h	45	6.2	−0.3	>0.3	20	5.4/5.6
1196A1	−32	−15	133	01^h	47	6.2	0.1	>0.3	15	6.0/4.7
1234A1	−15	−151	138	01^h	63	4.4	0.06	>0.3	15	4/4.9
1254A1	−15	43	141	01^h	64	4.2	0.15	>0.3	15	3.8/3.2
1258A1	−32	10	141	01^h	66	3.9	0.01	>0.3	20	4.1/3.4
1260A1	−32	173	142	00^h	55	9.1	0.16	>0.3	30	11/14.8
1305A1	−15	70	148	00^h	56	7.6	0.2	>0.3	30	12.3/10.3
1331A1	−15	33	152	00^h	57	4.7	−0.2	>0.3	25	5.2/5.6
1354A1	−15	−68	155	00^h	61	3.5	0.4	0.3	15	4.8/3.1

[a] z_{max} is the altitude of the cloud peak. Accordingly, σ_{max}, α, and R_{eff} are given for this altitude.
[b] σ_{max} is given at $\lambda = 250$ nm.
[c] Δz is the vertical extent of the cloud layer.
[d] τ_{250} and τ_{500} are the total optical depths of the cloud layer at $\lambda = 250$ and 500 nm, respectively.

sarily ruled out but do not appear in these restricted statistics. It is likely that isolated and geographically restricted thunderstorm events may not leave a detectable signature in an observation which integrates large spatial scales, as does an occultation.

[33] The presence of suspended particles that deep in the polar night is interesting. Figure 12 indicates that haze is composed of particles with α values greater than 2. Such α values, consistent with a particle radius no larger than 0.1–0.2 μm, are relatively high when compared to coefficients

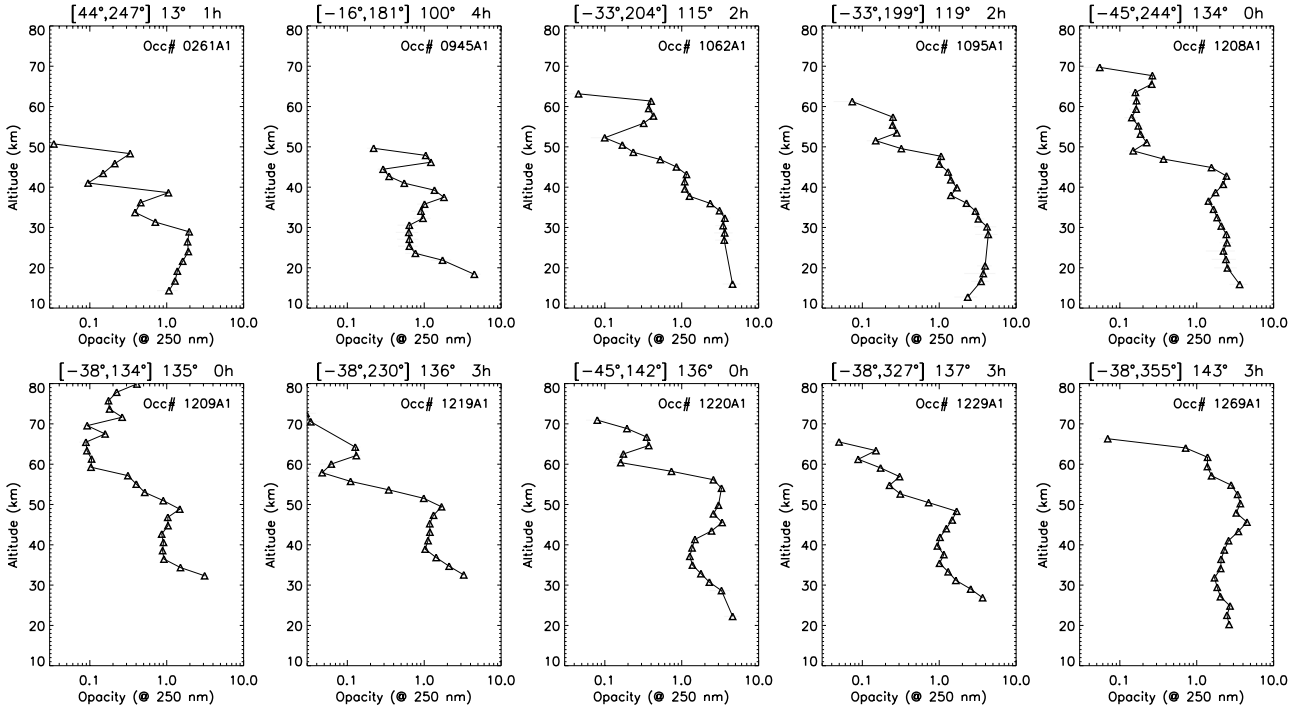

Figure 10. A subset of profiles exhibiting a distinct multilayer structure. Same presentation as in Figure 8, except that Angström coefficients that were omitted for clarity.

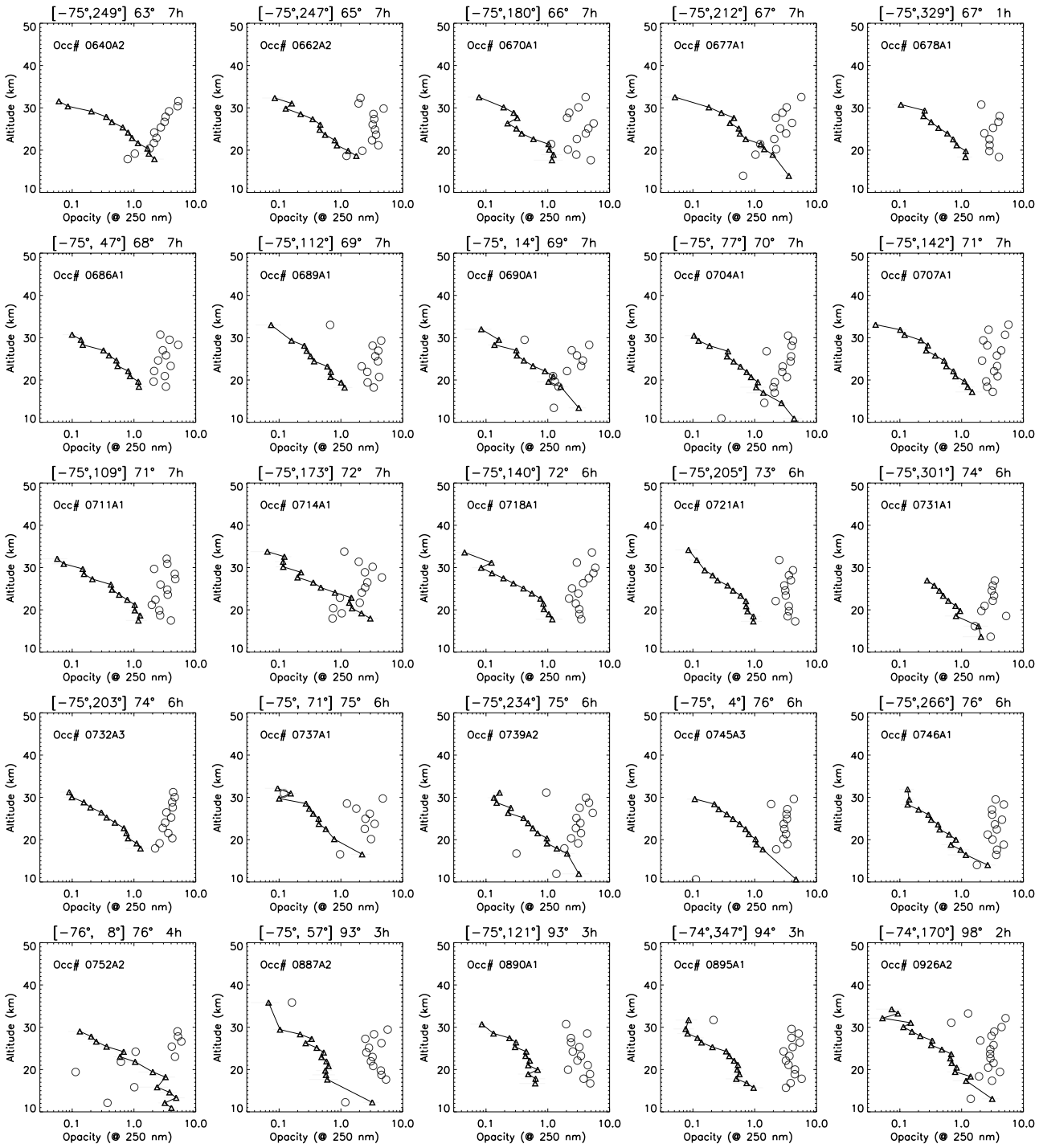

Figure 11. Same as in Figure 8 except that all profiles were collected poleward of 70°S. Observations sample the southern fall/winter and are thus representative of the haze profile in the southern hemisphere polar night.

obtained at comparable altitude but in other regions. The polar night haze is thus made of significantly smaller particles, suggesting that a specific microphysics is at work in this area. No spectral signature can be used to firmly conclude about particle composition. Clouds are, however, believed to dominate the polar night haze, a statement supported by the only relevant TES limb profile wherein water ice is spectrally identified as the unique haze component [*Pearl et al.*, 2001]. In addition, climate models usually predict water ice clouds with a vertical structure in qualitative agreement with the one observed [*Montmessin et al.*, 2004] (see Figure 13 for the corresponding GCM profile). If the haze observed by SPICAM happens to be made of dust, then our estimates on particle size may indicate the presence of an Aitken core population which has escaped nucleation and further scavenging by clouds.

[34] Total opacity can be estimated by extrapolating haze profiles down to the surface. This is done by fitting

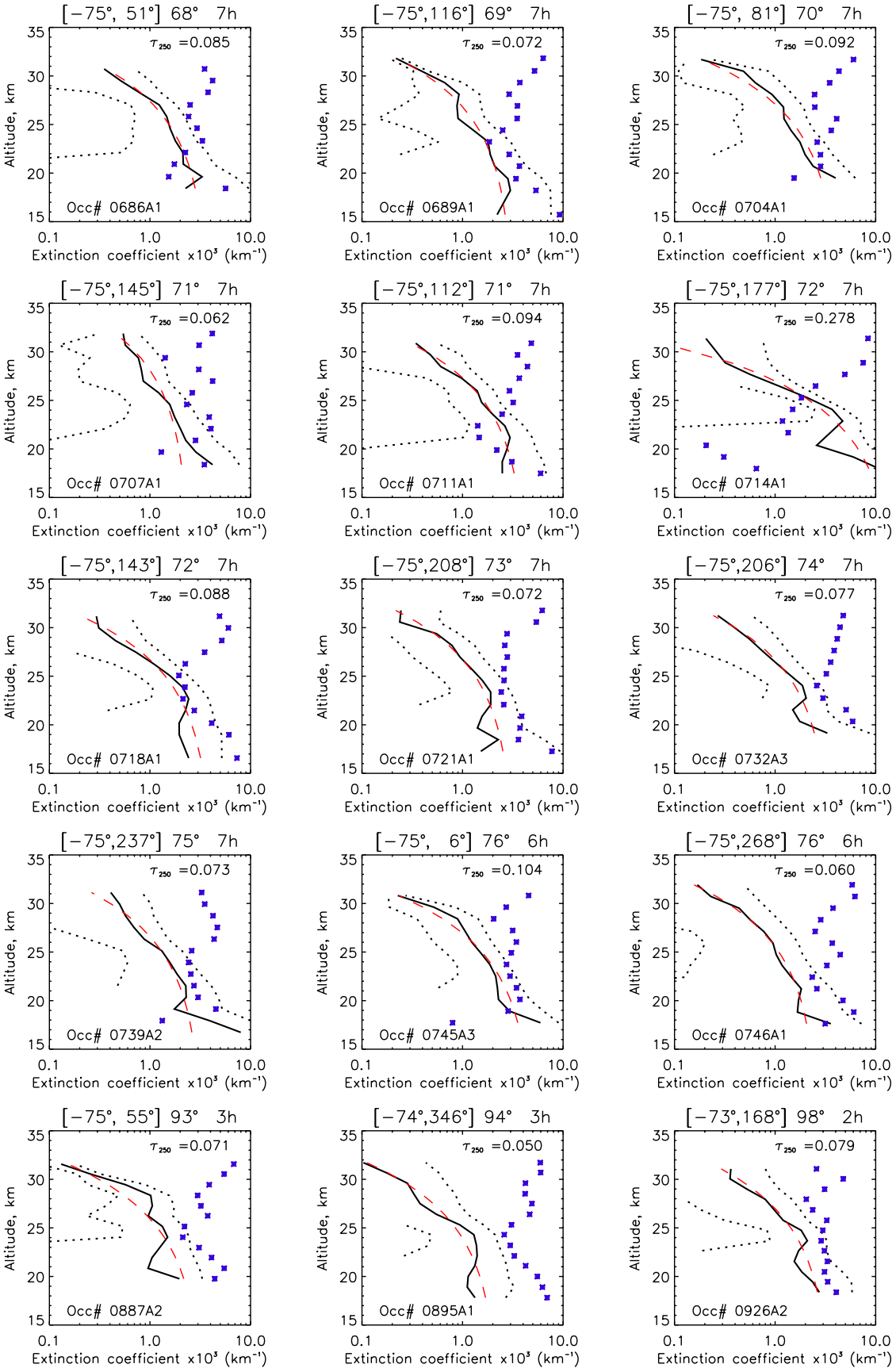
[−75°, 51°] 68° 7h
τ250 =0.085
Occ# 0686A1
[−75°,116°] 69° 7h
τ250 =0.072
Occ# 0689A1
[−75°, 81°] 70° 7h
τ250 =0.092
Occ# 0704A1
[−75°,145°] 71° 7h
τ250 =0.062
Occ# 0707A1
[−75°,112°] 71° 7h
τ250 =0.094
Occ# 0711A1
[−75°,177°] 72° 7h
τ250 =0.278
Occ# 0714A1
[−75°,143°] 72° 7h
τ250 =0.088
Occ# 0718A1
[−75°,208°] 73° 7h
τ250 =0.072
Occ# 0721A1
[−75°,206°] 74° 7h
τ250 =0.077
Occ# 0732A3
[−75°,237°] 75° 7h
τ250 =0.073
Occ# 0739A2
[−75°, 6°] 76° 6h
τ250 =0.104
Occ# 0745A3
[−75°,268°] 76° 6h
τ250 =0.060
Occ# 0746A1
[−75°, 55°] 93° 3h
τ250 =0.071
Occ# 0887A2
[−74°,346°] 94° 3h
τ250 =0.050
Occ# 0895A1
[−73°,168°] 98° 2h
τ250 =0.079
Occ# 0926A2
Altitude, km
Extinction coefficient x10³ (km⁻¹)

Figure 12

extinction profiles with the formula proposed by *Conrath* [1975] to replicate an aerosol distribution in balance with sedimentation and mixing processes:

$$\sigma_z = \sigma_o \exp(\gamma(1 - p_o/p_z))$$

where σ is the extinction coefficient at 250 nm at a level p_z. σ_o, the extinction coefficient at a reference level p_o, and γ, the so-called Conrath parameter, are tentatively adjusted. As shown by Figure 12, the Conrath representation proves particularly efficient at reproducing the typical structure of the polar night haze. Vertical integration of the above formula yields a typical optical depth of about 0.05–0.1 in UV. Corresponding Angström values ≥1 suggests that the haze is probably a factor of 2 or 4 thinner at visible wavelength.

[35] γ is an important parameter for climate models which generally force the dust vertical distribution according to Conrath's approximation [*Haberle et al.*, 1999; *Forget et al.*, 1999], except that the quantity of interest is the mass mixing ratio instead of the extinction coefficient. In order to help these models refine their prescription in the south polar night, we have performed additional fittings at a visible wavelength of 500 nm since most values for γ have been published in that range. We did this by extrapolating σ from 250 to 500 nm using the wavelength constraint given by Angström coefficients. We obtain γ values around 0.03–0.05 (the higher γ, the shallower the dust layer), slightly above the 0.03 value used by the NASA GCM model to match Pathfinder entry profile [*Haberle et al.*, 1999] and the 0.02 value derived from fitting the average extinction coefficient profile of the near-equatorial region (Figure 7, right plot), both being probably representative of typical weather conditions on Mars.

4. Discussion

[36] Retrievals of the Martian haze vertical profile prove scientifically rich. Data accumulated by SPICAM provide new insights into our understanding of Mars' climate. Our observations agree with the usual picture of a continuous dust haze covered by detached layers (of a likely condensate origin, although no spectral signatures can be used to support our speculations about composition). If our observations are an indirect evidence that the vertical extent of the haze is limited by cloud layers near the top, then it confirms that Martian clouds form on dust particles and that scavenging prevents dust from reaching higher altitudes (as originally modeled by *Michelangeli et al.* [1993]). Since dust dictates to a large extent the thermal structure, seasonal changes of temperature are reinforced by dust concentration changing with the cloud level drifting up and down. These microphysical interactions between cloud and dust particles remain an aspect of the Martian climate still unexplored, although possibly containing answers to the still unknown causes of interannual variability. Figure 4 illustrates this seasonal variation of the haze, with a difference of more than 30 km between the hazetop at aphelion and perihelion. Figure 5 further indicates a strong latitudinal disparity and reveals a highly confined haze layer in the winter polar regions. The nonlinear nature of cloud formation leads to the belief that microphysics can affect the radiative balance of the planet to the point that the climatic system is put into a precarious state of stability. This has been approached by *Rodin et al.* [1999], who specifically modeled the post-aphelion season and showed that slight changes in initial conditions may result in rapidly divergent climatic states.

[37] Our observations improve the database on Martian cloud properties, with the 25 occultation sequences which have been specifically selected for exhibiting putative cloud layers. These profiles are mostly concentrated in southern latitudes. In most cases, retrieved properties give a lower limit of 0.3 μm for the ice crystal radius. However, several cases give a robust estimate of around 0.1–0.2 μm which differs substantially from the 1 to 4 μm associated with type I and II clouds as categorized by *Clancy et al.* [2003] and *Wolff and Clancy* [2003] from TES visible to IR opacity ratios and emission phase functions. Type I clouds are

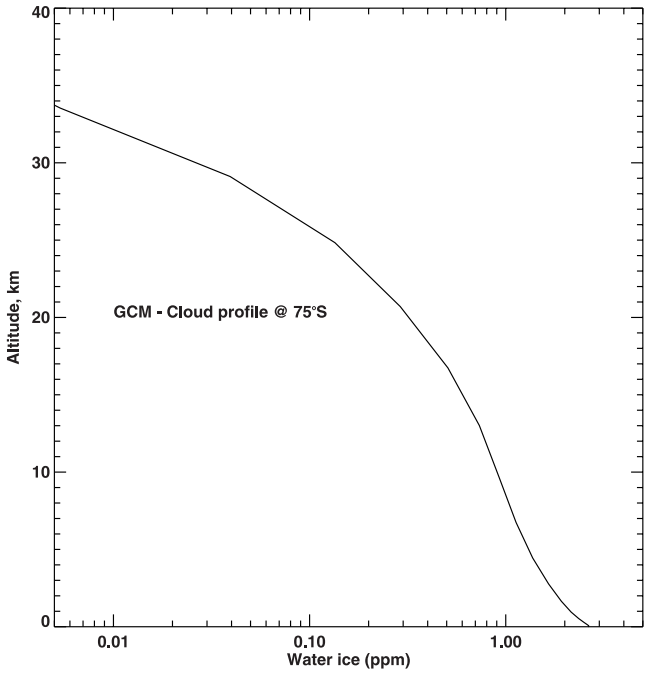

Figure 13. LMD-GCM predictions of the water ice cloud profile at 75°S around northern summer solstice (L_s 90°). The model predicts an atmospheric water ice content declining continuously throughout the atmosphere, in agreement with SPICAM observations.

Figure 12. Aerosol extinction profiles (solid curves) computed from the vertical inversion of a selection of opacity profiles (λ = 250 nm) obtained in the polar night and displayed in Figure 11. Dotted curves indicate measurement uncertainties at 1-σ. Blue crosses give the value of the Angström coefficient, whose values >1 suggest the presence of particles smaller than 0.2 μm in radius. Red dashed curves show vertical profiles of aerosol extinction obtained after fitting data with a Conrath approximation (see text for explanation). We also indicate the value of total UV opacity obtained from the vertical extrapolation of the fitted profile down to the surface.

composed of 1 to 2 μm crystals and are mostly found above 20 km in the southern aphelion hemisphere. Type II clouds exhibit twice larger crystal size and appear essentially within the aphelion cloud belt near the equator. The spectral signature of 1 to 4 μm crystals being rather neutral in the UV, differences between the two types cannot be sensed by SPICAM. SPICAM detection is more sensitive to the small radius tail of the particle size distribution since submicronic particle extinction maximizes at UV wavelength. Noteworthy, solar occultation profiles [*Chassefiere et al.*, 1992] performed during PHOBOS mission detected 5 cloud occurrences at or around an altitude of 50 km. PHOBOS cloud characteristics are similar as in our work, with ice crystals as small as 0.15 μm and opacities not exceeding a few hundredths. The 0.1 μm particle radius we have retrieved for some detached layers suggests the presence of a distinct class of clouds, type III using the classification introduced previously, associated with their unusually small crystal size and probably resulting from particular conditions of formation. Type III clouds should be found mostly in the upper atmosphere where the faster fall velocity prevents micron-sized particles to remain aloft and therefore favors size distributions centered on submicron values. In addition, condensation timescale significantly increases at higher altitudes where the rarefied atmosphere slows crystal diffusive growth. It is possible that smaller cloud particles also reflect the presence of more dust nuclei for water ice to condense onto. We can also mention that SPICAM has detected several detached layers up to a height of more than 100 km (as indicated by some points in Figure 4 scattered around 80 to 100 km at L_s 130 and 250°). However, these clouds belong to a distinct type, this time referring to their CO_2 composition. We discuss this in more detail elsewhere [*Montmessin et al.*, 2006].

[38] Another interesting finding stems from our analysis of the average behavior of the Martian haze (displayed in Figure 7). We distinguish two different types of haze profile which connect to their geographic locations: the near-equator regions and everywhere else. This may sound a little too restrictive, considering the variety of vertical structures noted in the observations. However, we had no success in our attempts to discriminate additional typical structures by averaging various geographical sectors. The average profile extracted from latitudes poleward of 15° indeed reveals a spike of opacity above 40 km, probably reflecting recurrent or long-lasting cold events leading to frequent cloud formations. Also, the near equator region (between 15°S and 15°N) theoretically lies all year long in the zone of the Hadley cell. The profile appearance of a haze in balance with sedimentation and mixing may thus be the relics of the more intense convective motions of the near-equatorial regions. However, care must be taken not to conclude too hastily given the incomplete seasonal and latitudinal coverage of our occultations.

[39] Surprisingly, the separation between the near-equator region and other latitudes does not hold at altitudes greater than 60 km. In this portion of the atmosphere, we find that the Martian haze has the same properties everywhere, exhibiting a smooth decrease of opacity up to 80 km while spectroscopy reveals the dominant presence of submicron particles. We suggest that these highly elevated fine particles reflect the long-term presence of a background population made of mineral dust. First, their small size increases their residence time and thus allows them to be more easily transported horizontally or vertically. Second, small size grains are less easily nucleated and thus are less frequently scavenged since their small radius increases curvature effect which in turn prevents rapid formation of water ice embryos at their surface. *Markiewicz et al.* [1999] inferred an increase of dust particle size with increasing wavelength from the analysis of Pathfinder images. *Markiewicz et al.* [1999] speculated about the presence of a submicron dust particle mode in addition to the canonical micron mode to explain this size drift. A secondary mode of fine particles was also needed to reproduce the diurnal peaks of opacity at blue wavelength detected by Pathfinder [*Smith and Lemmon*, 1999]. Finally, a similar "submicron hypothesis" has been proposed by *Montmessin et al.* [2002] using Viking limb profiles. Considering the great impact of dust on the temperature structure, we feel this submicronic mode is an important aspect of Mars microphysics. Besides, despite their low inclination for nucleation, submicron particles may eventually supply condensation supports at altitudes that would otherwise not be reached by the coarser micronic grain mode. This is important as our observations of cloud layers up to 100 km pose severe constraints on the need of cloud seeds at these heights. As it is probably the case on Earth, cloud formation may also benefit from the constant input of meteoritic debris and thus the origin of these small grains remain unresolved in the absence of more detailed spectroscopic observations.

[40] Information extracted by SPICAM from the polar night gives us new insights into the behavior of aerosols in this region. South winter pole haze is uniform and exhibits the same trends; a low opacity and the apparent signature of small particles, again lying in the submicronic range. A systematic comparison with models will give new perspectives on the seasonal evolution of the polar haze, which has a deep impact on Mars' climate as a whole. While previous observations and GCM results support a condensate origin for the haze, dust cannot be excluded.

[41] Finally, we shall stress out the upcoming analysis of solar occultation observations where both IR and UV channels work together. Water ice can be spectrally identified, along with water vapor while analysis of the continuum optical depth between 1 and 1.7 μm should allow us to constrain more accurately the size distribution of aerosols, possibly revealing multimodal functions. The present work and the promising analysis of UV and IR solar spectrum data prove how relevant the occultation technique is for the survey of planetary atmospheres.

[42] **Acknowledgments.** The authors thank two anonymous reviewers whose constructive criticism of the paper significantly strengthened the content of the manuscript. Mars Express is a space mission from ESA (European Space Agency). We wish to express our gratitude to all ESA members who participated in this successful mission, and in particular to the ESOC team for the delicate controlling of the spacecraft and René Pischel and Tanja Zeghers at ESTEC for careful planning exercises. We thank also Astrium Corp. for the design and construction of the spacecraft, and in particular Alain Clochet. We thank our collaborators at the three institutes for the design and fabrication of the instrument (Service d'Aéronomie/France, BIRA/Belgium, and IKI/Moscow), and in particular Emiel Van Raansbeck at BIRA for careful mechanical design. We also acknowledge the work of E. Dimarellis, A. Reberac, M. Barthelemy, and J. F. Daloze, who handle SPICAM operations at Service d'Aéronomie. We wish to thank CNRS and CNES for financing SPICAM in France and the Space

Division of the Belgian Federal Science Policy Office for supporting this project through the ESA PRODEX program. The Russian team acknowledges support of RFFI grant 04-02-16856-a.

References

Anderson, E., and C. Leovy (1978), Mariner 9 television limb observations of dust and ice hazes on Mars, *J. Atmos. Sci.*, *35*, 723–734.

Bertaux, J. L., et al. (2000), The study of the Martian atmosphere from top to bottom with SPICAM light on Mars Express, *Planet. Space Sci.*, *48*, 1303–1320.

Bertaux, J.-L., et al. (2006), SPICAM on board Mars Express: Instrument, operations, observing modes, and overview of typical results, *J. Geophys. Res.*, doi:10.1029/2006JE002690, in press.

Chassefiere, E., and J. E. Blamont (1992), Vertical transport of water ice at low latitudes in the Martian atmosphere, *Geophys. Res. Lett.*, *19*, 945–948.

Chassefiere, E., J. E. Blamont, V. A. Krasnopolsky, O. I. Korablev, S. K. Atreya, and R. A. West (1992), Vertical structure and size distributions of Martian aerosols from solar occultation measurements, *Icarus*, *97*, 46–69, doi:10.1016/0019-1035(92)90056-D.

Clancy, R. T., A. W. Grossman, M. J. Wolff, P. B. James, D. J. Rudy, Y. N. Billawala, B. J. Sandor, S. W. Lee, and D. O. Muhleman (1996), Water vapor saturation at low latitudes around aphelion: A key to Mars climate?, *Icarus*, *122*, 36–62.

Clancy, R. T., M. J. Wolff, and P. R. Christensen (2003), Mars aerosol studies with the MGS TES emission phase function observations: Optical depths, particle sizes, and ice cloud types versus latitude and solar longitude, *J. Geophys. Res.*, *108*(E9), 5098, doi:10.1029/2003JE002058.

Colaprete, A., R. M. Haberle, and O. B. Toon (2003), Formation of convective carbon dioxide clouds near the south pole of Mars, *J. Geophys. Res.*, *108*(E7), 5081, doi:10.1029/2003JE002053.

Conrath, B. J. (1975), Thermal structure of the Martian atmosphere during the dissipation of dust storm 1971, *Icarus*, *24*, 34–46.

Dubovik, O., A. Smirnov, B. N. Holben, M. D. King, Y. J. Kaufman, T. F. Eck, and I. Slutsker (2000), Accuracy assessments of aerosol optical properties retrieved from Aerosol Robotic Network (AERONET) Sun and sky radiance measurements, *J. Geophys. Res.*, *105*(D8), 9791–9806.

Forget, F., F. Hourdin, R. Fournier, C. Hourdin, O. Talagrand, M. Collins, S. R. Lewis, P. L. Read, and J. Huot (1999), Improved general circulation models of the Martian atmosphere from the surface to above 80 km, *J. Geophys. Res.*, *104*, 24,155–24,176.

Haberle, R. M., M. M. Joshi, J. R. Murphy, J. R. Barnes, J. T. Schofield, G. Wilson, M. Lopez-Valverde, J. L. Hollingsworth, A. F. C. Bridger, and J. Schaeffer (1999), General circulation model simulations of the Mars Pathfinder atmospheric structure investigation/meteorology data, *J. Geophys. Res.*, *104*, 8957–8974.

Hess, S. L. (1973), Martian winds and dust clouds, *Planet. Space Sci.*, *21*, 1549–1557, doi:10.1016/0032-0633(73)90061-5.

Hinson, D. P., R. J. Wilson, M. D. Smith, and B. J. Conrath (2003), Stationary planetary waves in the atmosphere of Mars during southern winter, *J. Geophys. Res.*, *108*(E1), 5004, doi:10.1029/2002JE001949.

Jaquin, F., P. Gierasch, and R. Kahn (1986), The vertical structure of limb hazes in the Martian atmosphere, *Icarus*, *68*, 442–461, doi:10.1016/0019-1035(86)90050-3.

Korablev, O. I., V. A. Krasnopolsky, A. V. Rodin, and E. Chassefiere (1993), Vertical structure of Martian dust measured by solar infrared occultations from the PHOBOS spacecraft, *Icarus*, *102*, 76–87, doi:10.1006/icar.1993.1033.

Korablev, O., V. I. Moroz, E. V. Petrova, and A. V. Rodin (2005), Optical properties of dust and the opacity of the Martian atmosphere, *Adv. Space Res.*, *35*, 21–30, doi:10.1016/j.asr.2003.04.061.

Lebonnois, S., E. Quémerais, F. Montmessin, F. Lefèvre, S. Perrier, J.-L. Bertaux, and F. Forget (2006), Vertical distribution of ozone on Mars as measured by SPICAM/Mars Express using stellar occultations, *J. Geophys. Res.*, doi:10.1029/2005JE002643, in press.

Markiewicz, W. J., R. M. Sablotny, H. U. Keller, N. Thomas, D. Titov, and P. H. Smith (1999), Optical properties of the Martian aerosols as derived from Imager for Mars Pathfinder midday sky brightness data, *J. Geophys. Res.*, *104*(E4), 9009–9018.

Michelangeli, D. V., O. B. Toon, R. M. Haberle, and J. B. Pollack (1993), Numerical simulations of the formation and evolution of water ice clouds in the Martian atmosphere, *Icarus*, *100*, 261–285.

Montmessin, F., P. Rannou, and M. Cabane (2002), New insights into Martian dust distribution and water-ice cloud microphysics, *J. Geophys. Res.*, *107*(E6), 5037, doi:10.1029/2001JE001520.

Montmessin, F., F. Forget, P. Rannou, M. Cabane, and R. M. Haberle (2004), Origin and role of water ice clouds in the Martian water cycle as inferred from a general circulation model, *J. Geophys. Res.*, *109*, E10004, doi:10.1029/2004JE002284.

Montmessin, F., et al. (2006), Subvisible CO_2 ice clouds detected in the mesosphere of Mars, *Icarus*, *183*(2), 403–410.

Ockert-Bell, M. E., J. F. Bell III, J. B. Pollack, C. P. McKay, and F. Forget (1997), Absorption and scattering properties of the Martian dust in the solar wavelengths, *J. Geophys. Res.*, *102*(E4), 9039–9050.

O'Neill, N., and A. Royer (1993), Extraction of bimodal aerosol-size distribution radii from spectral and angular slope (Angstrom) coefficients, *Appl. Opt.*, *32*, 1642–1645.

Pang, K., and J. M. Ajello (1977), Complex refractive index of Martian dust—Wavelength dependence and composition, *Icarus*, *30*, 63–74.

Parkinson, W. H., J. Rufus, and K. Yoshino (2003), Absolute cross section measurements of CO_2 in the wavelength region 163–200 nm and the temperature dependence, *Chem. Phys.*, *219*, 45–57.

Pearl, J. C., M. D. Smith, B. J. Conrath, J. L. Bandfield, and P. R. Christensen (2001), Observations of Martian ice clouds by the Mars Global Surveyor Thermal Emission Spectrometer: The first Martian year, *J. Geophys. Res.*, *106*(E6), 12,325–12,338.

Pollack, J. B., and J. N. Cuzzi (1980), Scattering by nonspherical particles of size comparable to wavelength—A new semi-empirical theory and its application to tropospheric aerosols, *J. Atmos. Sci.*, *37*, 868–881.

Pollack, J. B., D. S. Colburn, F. M. Flasar, R. Kahn, C. E. Carlston, and D. G. Pidek (1979), Properties and effects of dust particles suspended in the Martian atmosphere, *Planet. Space Sci.*, *84*(13), 2929–2945.

Pollack, J. B., M. E. Ockert-Bell, and M. K. Shepard (1995), Viking Lander image analysis of Martian atmospheric dust, *J. Geophys. Res.*, *100*, 5235–5250.

Quémerais, E., J.-L. Bertaux, O. Korablev, E. Dimarellis, C. Cot, B. R. Sandel, and D. Fussen (2006), Stellar occultations observed by SPICAM on Mars Express, *J. Geophys. Res.*, doi:10.1029/2005JE002604, in press.

Rafkin, S. C. R., M. R. V. Sta. Maria, and T. I. Michaels (2002), Simulation of the atmospheric thermal circulation of a Martian volcano using a mesoscale numerical model, *Nature*, *419*, 697–699.

Rannou, P., S. Perrier, J.-L. Bertaux, F. Montmessin, O. Korablev, and A. Rébérac (2006), Dust and cloud detection at the Mars limb with UV scattered sunlight with SPICAM, *J. Geophys. Res.*, doi:10.1029/2006JE002693, in press.

Rodin, A. V., R. T. Clancy, and R. J. Wilson (1999), Dynamical properties of Mars water ice clouds and their interactions with atmospheric dust and radiation, *Adv. Space Res.*, *23*, 1577–1585.

Smith, M. D. (2004), Interannual variability in TES atmospheric observations of Mars during 1999–2003, *Icarus*, *167*, 148–165.

Smith, M. D., J. C. Pearl, B. J. Conrath, and P. R. Christensen (2001), Thermal Emission Spectrometer results: Mars atmospheric thermal structure and aerosol distribution, *J. Geophys. Res.*, *106*(E10), 23,929–23,945.

Smith, P. H., and M. Lemmon (1999), Opacity of the Martian atmosphere measured by the Imager for Mars Pathfinder, *J. Geophys. Res.*, *104*(E4), 8975–8986.

Tamppari, L. K., R. W. Zurek, and D. A. Paige (2000), Viking era water-ice clouds, *J. Geophys. Res.*, *105*, 4087–4107.

Tomasko, M. G., L. R. Doose, M. Lemmon, P. H. Smith, and E. Wegryn (1999), Properties of dust in the Martian atmosphere from the Imager on Mars Pathfinder, *J. Geophys. Res.*, *104*(E4), 8987–9008.

Warren, S. G. (1984), Optical constants of ice from the ultraviolet to the microwave, *Appl. Opt.*, *23*, 1206–1225.

Warren, S. G. (1986), Optical constants of carbon dioxide ice, *Appl. Opt.*, *25*, 2650–2674.

Wolff, M. J., and R. T. Clancy (2003), Constraints on the size of Martian aerosols from Thermal Emission Spectrometer observations, *J. Geophys. Res.*, *108*(E9), 5097, doi:10.1029/2003JE002057.

Yoshino, K., J. R. Esmond, Y. Sun, W. H. Parkinson, K. Ito, and T. Matsui (1996), Absorption cross section measurements of carbon dioxide in the wavelength region 118.7 nm–175.5 nm and the temperature dependence, *J. Quant. Spectrosc. Radiat. Transfer*, *50*, 53–60.

J. L. Bertaux, F. Montmessin, E. Quémerais, and P. Rannou, Service d'Aéronomie du CNRS/IPSL, Réduit de Verrières, Route des Gatines, F-91371 Verrières le Buisson Cédex, France. (franck.montmessin@aero.jussieu.fr)

O. Korablev, Space Research Institute (IKI), 84/32 Profsovuznava, 117810 Moscow, Russia.

S. Lebonnois, Laboratoire de Météorologie Dynamique, IPSL, CNRS/UPMC, Box 99, F-75252 Paris Cédex 05, France.